



# Stress tensor mesostructures for deterministic figuring of thin substrates

YOUWEI YAO,<sup>1</sup> BRANDON CHALIFOUX,<sup>2</sup> RALF K. HEILMANN,<sup>1</sup> AND MARK L. SCHATTENBURG<sup>1,\*</sup>

<sup>1</sup>Space Nanotechnology Laboratory, MIT Kavli Institute for Astrophysics and Space Research, Massachusetts Institute of Technology, 77 Massachusetts Avenue, Cambridge, Massachusetts 02139, USA

<sup>2</sup>James C. Wyant College of Optical Sciences, The University of Arizona, 1630 E. University Blvd., Tucson, Arizona 85721-0094, USA

\*Corresponding author: marks@space.mit.edu

Received 7 October 2021; revised 9 February 2022; accepted 2 March 2022; published 14 April 2022

Accessing the immense value of freeform surfaces for mass-sensitive applications such as space optics or metaform optical components requires fabrication processes that are suited to figuring thin substrates. We present stress tensor mesostructures for precisely correcting figure errors, even after microstructures or coatings have been applied to the optical surface. These mesostructures can be fabricated using standard semiconductor fabrication equipment. We introduce three different mesostructure types that each spatially control the three required stress tensor components over the surface of thin substrates, each offering relative advantages. We patterned all three mesostructures on the backsides of silicon wafers to demonstrate freeform figure generation and correction. Stress tensor mesostructures can enable low-cost accurate figuring of the thin substrates that will become increasingly important for lightweight and metasurface optics. © 2022 Optica Publishing Group under the terms of the [Optica Open Access Publishing Agreement](https://doi.org/10.1364/OPTICA.445379)

<https://doi.org/10.1364/OPTICA.445379>

## 1. INTRODUCTION

The recent explosion in metasurface optics research [1–3] promises to drive optical systems toward lighter and simpler systems with exciting new capabilities. Meanwhile, the rapidly growing set of techniques to make accurate freeform mirror surfaces [4] has resulted in more compact optical systems that use fewer components than was ever possible before. Combining meta-lenses with thin freeform mirrors [1] provides synergy to create ultralightweight folded optical systems that will become ever more important as wearable optical systems such as augmented reality headsets [5] become ubiquitous, or as more optical systems are launched into space [6–8]. A barrier to accessing this synergy is that current optical fabrication methods are unsuitable for figuring thin freeform mirrors because they uncontrollably bend thin mirror substrates during fabrication [6,9], and since they remove material from the optical surface they must be used before microstructures and thin reflective films are created. Noncontact deterministic figuring techniques that leave the optical surface unaffected could open the door to freeform metasurface optics, improve the figure accuracy of deformable mirrors [10,11] and semiconductor wafers [12,13], and enable ultrathin mirrors for space applications [10,11,14,15].

In all of these applications, the substrate should be deterministically and permanently figured after coatings, active device layers, or microstructures have been created. Material removal and additive processes such as polishing [9], chemical and plasma etching [16], ion-beam figuring [14], and 3D-printing [17] can accurately figure surfaces but generate residual stresses that create unexpected deformations of thin substrates [9]. In addition, forming thin

substrates with a functionalized surface is almost impossible using these methods due to the stress in coatings, structures, and device layers.

In contrast to material removal processes, stress figuring processes create stress on the back surface to bend the substrate [15,18,19] and leave the optical surface unaffected. Flat or curved substrates can be coated and accurately patterned using ultraviolet lithography [18,19]. Stress can be readily generated using a wide variety of coating materials suitable for specific applications: piezoelectric or magnetostrictive [9,11] films for dynamic deformation and metal or dielectric thin films [18,20] for set-and-forget figuring. Most existing stress generation methods are limited to only correcting a subset of figure errors or small clear apertures [21] because the stress is uniaxial (e.g., equibiaxial stress or uniaxial stress with fixed orientation) [22] (Fig. S1). Generating arbitrary deformation requires fully controlling all three in-plane stress tensor components, i.e., the two normal stresses ( $\sigma_x$ ,  $\sigma_y$ ) and shear stress ( $\tau_{xy}$ ). Existing methods to provide the required nonequibiaxial stress control include ion implantation [15], laser processing [23], and 3D-printing with ferromagnetic or ferroelectric powders [24,25], but these methods rely on difficult-to-control and spatially varying process parameters (ion dose, write speed, droplet size, etc.) that degrade stress manipulation accuracy. Stable methods to precisely control the stress state over the back surface of a thin substrate are necessary but still lacking.

We present three types of mesostructures (Fig. 1) to fully control the stress state over the entire substrate back surface, relying primarily on patterning accuracy. We designed and patterned three types of mesostructures on the backside of 100 mm silicon wafers

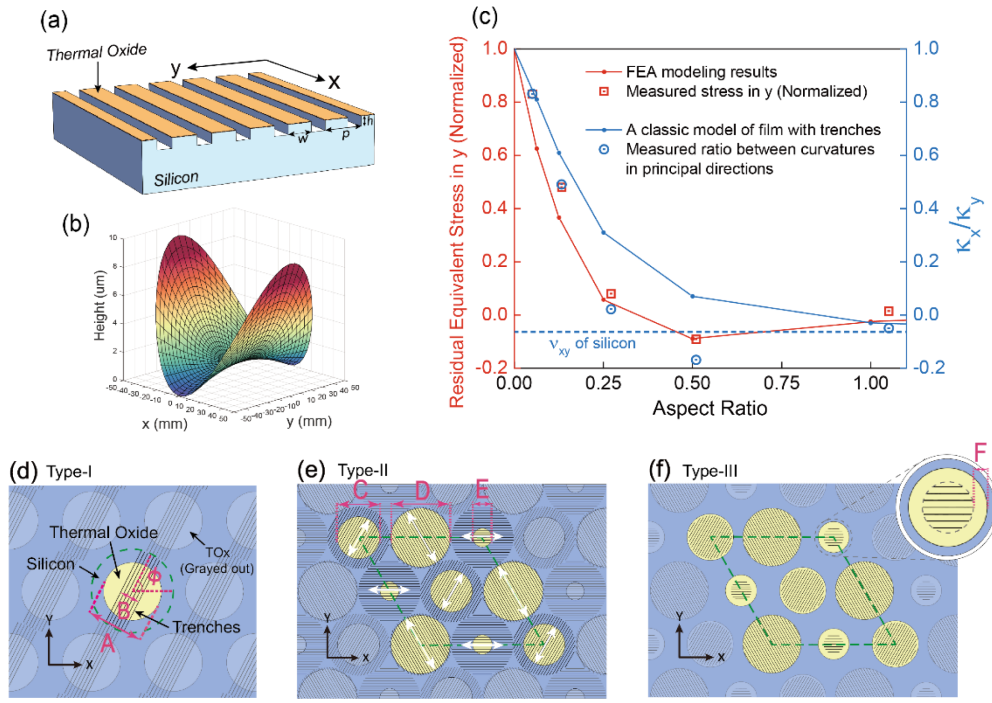


**Fig. 1.** (a) Grating lines trenched into silicon substrates, with the TOx coated on the top of the grating tooth.  $AR = h/w$ ; the thickness of TOx is negligible. (b) Measured deformation of a silicon wafer. Backside is patterned by a uniform grating structure in (a) with  $AR = 0.5$ . (c) The red line and squares represent the modeled and measured equivalent stress (normalized by the stress when  $AR = 0$ ) in the  $y$  direction, assuming the grating structure in (a) is a fictitious equivalent continuous film. The blue line and circles show the ratio of the curvatures between the  $x$  and  $y$  directions on a grating-patterned silicon wafer. The blue line shows a theoretical result from a classic model, in which the trenches are only in the film [26] ( $AR = h/w$  for teeth of coatings, width comparable with the coating thickness). The blue circles are the measured results ( $AR = h/w$  for teeth of trenched silicon, width much larger than the coating thickness). The dashed blue line is the asymptotic line of the solid line derived from the classic model, with the value of silicon's Poisson's ratio,  $\nu_{xy}$ . (d) Type-I mesostructure with a highlighted exemplar unit cell at the center. The yellow disk is a 200 nm-thick TOx layer. The blue area by TOx is bare silicon. The parallel lines are trenched gratings through TOx into the silicon substrate. The grating line pitch is 10  $\mu\text{m}$ , and the aspect ratio of the grating tooth is 1. Parameters  $A$ ,  $B$ , and  $\phi$  define the dimensions, which can vary from cell to cell within the boundary, which is a 500- $\mu\text{m}$ -diameter circle shown by the green dashed line. (Note: all TOx outside the highlighted unit cell region is grayed out.) (e) Type-II mesostructure with highlighted unit cell indicated by green dashed lines. The diameter of each grating circle area is 500  $\mu\text{m}$ , and the grating line pitch is 10  $\mu\text{m}$ . The orientations of the grating lines are fixed at  $-60^\circ$ ,  $0^\circ$ , and  $60^\circ$ , as noted by the white arrows. Parameters  $C$ ,  $D$ , and  $E$  represent TOx disk diameters that have different grating orientations. (f) Type-III mesostructures are similar to Type-II except the TOx disks are larger than the circled grating areas to provide additional equibiaxial stress by adjusting parameter  $F$ . The grating lines are trenched before the TOx growth and patterning process. Note that the side wall and the adjacent area of the grating teeth are also coated with TOx. As a result, the magnitude of the uniaxial stress produced by the grating area is increased, proportional to the AR.

to demonstrate precise, free-standing, full aperture figure generation and correction. The stress is provided by a thermally grown silicon dioxide layer on top of the structure, which is well known to be stable [18]. The demonstrated technique can be applied to fabricate thin mirrors using standard semiconductor equipment. The mesostructures we present can also apply to other stress generation methods including stressed coatings and functional materials for active deformation.

## 2. GENERATION OF UNIAXIAL STRESS

A state of plane stress (two normal stresses and a shear stress) can be decomposed into equibiaxial stress ( $\sigma_{\text{equi}}$ ) and uniaxial stress ( $\sigma_{\text{uni},j}$ ) components at a set of specific orientations ( $\phi_j$ ) by inverting Eq. (1):

$$\begin{bmatrix} \sigma_x \\ \sigma_y \\ \tau_{xy} \end{bmatrix} = \sum_{j=1}^m \begin{bmatrix} \cos^2(\phi_j) & \sin^2(\phi_j) & 2 \cos(\phi_j) \sin(\phi_j) \\ \sin^2(\phi_j) & \cos^2(\phi_j) & -2 \cos(\phi_j) \sin(\phi_j) \\ -\cos(\phi_j) \sin(\phi_j) & \cos(\phi_j) \sin(\phi_j) & \cos^2(\phi_j) - \sin^2(\phi_j) \end{bmatrix} \begin{bmatrix} \sigma_{\text{equi}} + \sigma_{\text{uni},j} \\ \sigma_{\text{equi}} \\ 0 \end{bmatrix}. \quad (1)$$

Here, the term on the left is a stress state represented in  $x - y$  coordinates. The terms on the right are the product of a three-by-three rotation matrix and a stress state vector in the principal coordinate frame (wherein the shear stress is zero; see Fig. S2). The summation limit  $m$  depends on the mesostructure type and will be explained later.

Equibiaxial stress already exists in conventional coatings. Here we present a scheme to create uniaxial stress as follows and illustrated in Figs. 1(a)–1(c). First, we coat a substrate with a film of equibiaxial stress. Second, we pattern the coated surface with grating lines in which trenches are extended into the substrate, in contrast with previous research that patterned the film only [26]. Our study has revealed that uniaxial stress can be generated with a grating pitch close to the total trench depth, which can be significantly greater than the thickness of the film. This relaxation

of the requirement on the grating pitch allows the patterns to be more easily manufactured.

Figure 1(a) illustrates an example of grating lines patterned horizontally ( $x$  direction) on the backside of a 100-mm-diameter, 0.5-mm-thick silicon wafer. The pitch is 10  $\mu\text{m}$ , much larger than the thickness of the stressed film—a 200-nm-thick thermally grown silicon dioxide (TOx) layer with  $-350$  MPa equibiaxial compressive stress. By using a 2D finite-element (FE) model (Fig. S3), we determined how the local bending curvature of the wafer surface in the  $y$  direction varies with the trench depth in silicon. After modeling, it is instructive to assume the grating structure can be replaced by a fictitious film of uniform stress, wherein the equivalent uniaxial stress of the film in the  $y$  direction is calculated from the wafer curvature for different aspect ratios ( $\text{AR} = h/w$ ; the thickness of the TOx is negligible) of the grating teeth, and then normalized to one for an AR of 0. The results are plotted as the red solid line in Fig. 1(c), suggesting that the equivalent film stress in the  $y$  direction drops to 0 when the AR is around 0.3 and greater than 1. In Section 3, we detail how patterns are created with fixed  $\text{AR} = 1$ , but with varying area, to linearly adjust equivalent integrated stress. On the other hand, a surprising stress reversal occurs when the AR is higher than 0.3, reaching a maximum when  $\text{AR} = 0.5$ . This stress reversal is not critical to the present work, which uses  $\text{AR} = 1$ . However, we have confirmed the presence of this stress reversal using FE models (Fig. S3) and additional experiments (Fig. S6). Further investigation and applications will be implemented in future work.

To test the modeled results, we patterned uniform grating lines with deep trenches on the backsides of five silicon wafers. Each wafer had the same 10  $\mu\text{m}$  grating pitch, but the trench depths produced by deep reactive ion etching varied with ARs from 0 to 1. The wafer deformation induced by the grating patterns was monitored by a Shack-Hartmann (S-H) metrology tool [27–29] (for details, see Fig. S4). Figure 1(b) shows an example of the measured deformation when  $\text{AR} = 0.5$ . Based on these measurements (Fig. S5), the normalized equivalent stresses in the  $y$  direction were calculated, with results plotted in Fig. 1(c) (red squares), matching the modeled results (solid red line) (Fig. S3). We have concluded that controlled uniaxial stress can be created when the AR is around 0.3. In addition,  $\text{AR} > 1.0$  can also produce nearly uniaxial stress.

We also measured the ratio of the curvatures between the  $x$  and  $y$  directions on the fabricated wafers (blue circles), comparing the results with a classic model (blue line), which has a similar configuration but assumes the trenches are only in the film [26]. The deviation demonstrates that bending due to the new method, i.e., a grating with substrate trenches, can converge to uniaxial stress faster and produce counterintuitive negative bending (Fig. S6).

### 3. CONTROL OF STRESS TENSOR WITH MESOSTRUCTURES

Based on this new capability of generating controlled uniaxial stress, we have created three types of periodic mesostructures arrayed in a 2D lattice on the backside of silicon wafers to produce stress tensors for freeform surface shaping. This scheme assumes that the mesostructures are comparable to, or smaller than, the substrate thickness, so that each unit cell can essentially be considered as a pixel of controllable stress representing a continuous tensor stress field. This scheme also prevents print-through from backside patterns [19] (Fig. S3). We present the three types of

mesostructures, with a set of parameters such as ( $A, B, \phi$ ) shown in Fig. 1(d), that are determined for each pixel by the stress tensor required to produce the desired substrate deformation. Figure 1(d) shows the Type-I mesostructure arrayed in a hexagonal lattice of 500  $\mu\text{m}$  horizontal spacing. The highlighted yellow disk of diameter  $A$  represents a pattern of the TOx layer. The ratio of the disk area to the unit cell area is controlled to determine the local magnitude of equibiaxial stress. The parallel lines with 10  $\mu\text{m}$  pitch represent trenches with  $\text{AR} = 1$  through the TOx into the silicon, which convert the stress within the grating area from equibiaxial to uniaxial, as discussed previously. The width  $B$  of the grating region controls the local magnitude of uniaxial stress, while the spin angle  $\phi$  controls its local orientation [see Eq. (1)].

After determining the target surface deformation, the desired stress is transformed from global orientation ( $\sigma_x, \sigma_y, \tau_{xy}$ ) to local orientation ( $\sigma_{\text{equi}}, \sigma_{\text{uni},j}, \phi_j$ ) using Eq. (1) (Fig. S2). For Type-I structures,  $m = 1$ , and  $\phi_1$  is the orientation of the grating lines,  $\sigma_{\text{equi}}$  is the equibiaxial stress, and  $\sigma_{\text{uni},1}$  is the uniaxial stress. These local stress states can be transformed, in turn, into 2D distributions of local geometric parameters  $A, B$ , and  $\phi$  using a calibration process (Figs. S7 and S8). Tensile and compressive stress components can be achieved by adding a bias film on the front and/or back surfaces (Figs. S6 and S9).

Type-I structures can produce deformations efficiently since grating lines in each unit cell are rotationally aligned to maximize the principal stresses. However, secondary adjustment of the stress orientation for post-correction deformation or shape actuation would be difficult. For this reason, we introduced the Type-II mesostructure as shown in Fig. 1(e). The unit cell is highlighted and indicated by green dashed lines consisting of a triplet of unique patterned circles. In this pattern,  $m = 3$  in Eq. (1), and  $\phi_j$  is one of the three grating line orientations ( $60^\circ, 0^\circ$ , or  $-60^\circ$ ),  $\sigma_{\text{equi}} = 0$ , and  $\sigma_{\text{uni},j}$  is the uniaxial stress (recall that  $j$  indicates the location of the cell on the substrate). In contrast with the Type-I mesostructure, the geometric variables of Type II are the diameters of the TOx disks at the three orientations [ $C, D$ , and  $E$  in Fig. 1(e)], which can manipulate the stress tensor components without changing the grating line orientations. This configuration can enable secondary adjustment (see Fig. 5) or active control of the stress tensor if the stress provider is a ferromagnetic or piezoelectric material. Although Type II has more flexibility, the magnitude of the stress generated is less than Type I since only one-third of the fractional TOx area is in effect at an arbitrary orientation.

We also developed a Type-III structure depicted in Fig. 1(f) for the purpose of producing higher magnitude stresses with comparable flexibility to the Type-II structure. The Type-III structure has grating lines with TOx also coated on the side walls and floors of grating teeth, providing additional uniaxial stresses proportional to the AR of the grating structure. Sidewall coatings can be realized by isotropic deposition methods after etching of grating lines, such as thermal oxidation or atomic layer deposition (ALD). However, these methods coat the area between grating teeth at the same time, producing undesired equibiaxial stress that can counteract the desired deformation. Therefore, the configuration of the Type-III structure was modified to resolve the problem. The diameters of the grating disks are controlled as variables for desired uniaxial stresses. The TOx disk patterned after deposition is slightly larger than the grating circles. The marginal ring of the TOx in each disk, indicated by  $F$ , produces an additional equibiaxial stress to even out the variation of equibiaxial stress generated by grating disks.

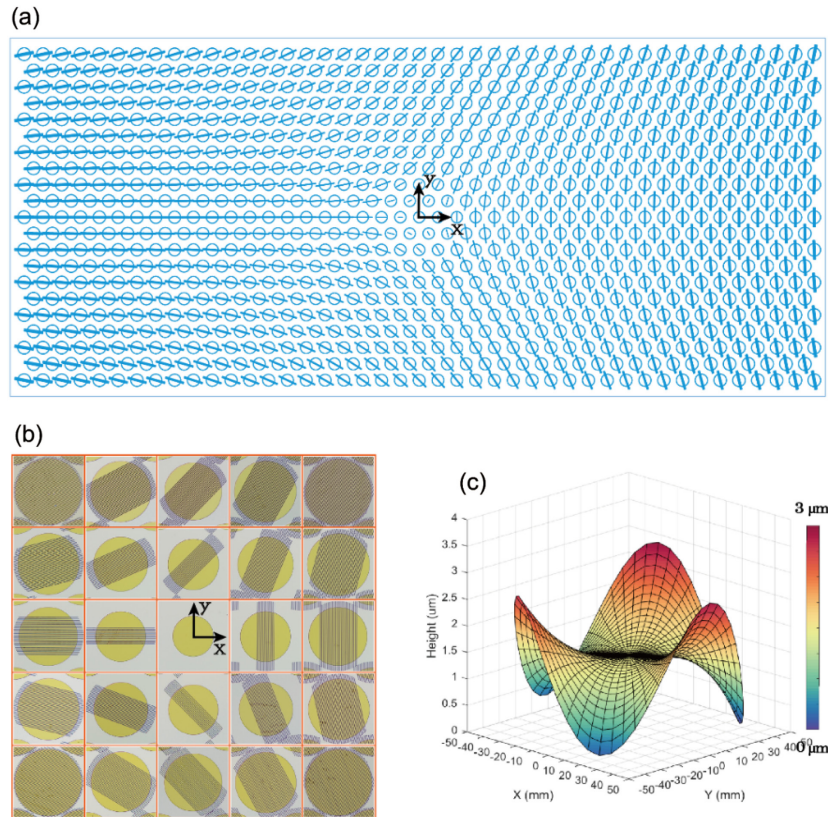


**Fig. 2.** (a) Portion of the design for generating trefoil deformation. The pitch between two adjacent circles is 500  $\mu\text{m}$ . (b) Microscope images of 25 fabricated individual unit cells for trefoil deformation. The cells are evenly distributed within a 70 mm by 70 mm area. (c) Measured wafer trefoil deformation.

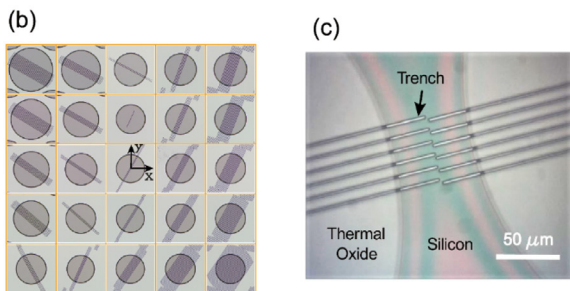
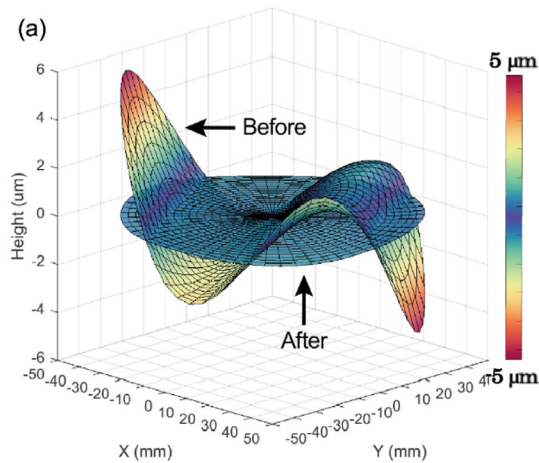


**Fig. 3.** (a) Measured wafer surface before (S shape) and after (flat shape) the patterning process. (b) Microscope images of 25 unit cells for flattening a wafer's surface. (c) Microscope image of the area between two unit cells.

Therefore, the equibiaxial stress within each disk is constant, which can be compensated by a uniform coating from the other side of the thin substrate for the initial demonstration in this work.

#### 4. DETERMINISTIC FIGURE GENERATION AND CORRECTION

To demonstrate the effective use of a Type-I structure for figure correction, we patterned the backsides of two free-standing silicon wafers to generate deterministic freeform deformations. We selected the Zernike term trefoil ( $Z_3^3$ ) as a deformation target since it requires uniaxial stress with varying magnitude and orientation [Eq. (S2)], which requires the manipulation of stress tensors beyond the conventional equibiaxial type. As for metrology, we measured the surface of all wafers using a S-H metrology tool [27–29] (Fig. S4), with measurement precision better than 10 nm RMS.

Figure 2(a) shows a portion of the structure design for trefoil deformation near the substrate center [Eq. (S3)–(S5)]. A 200-nm-thick TOx layer was used as a stress provider. Figure 2(b) shows 25 microscope images of individual unit cells evenly distributed within a 70 mm by 70 mm area. The measured deformation [Fig. S10] is represented by 12 Zernike polynomial terms (see green triangles in Fig. 4). Figure 2(c) shows the measured deformation, which demonstrates that trefoil has been successfully generated.

Ultraflat thin substrates are in demand for wide applications such as semiconductor manufacturing and metamaterial lenses. For a final demonstration, we selected a silicon wafer and then patterned an engineered Type-I backside structure designed to flatten the surface. In theory, controlling all three stress tensor

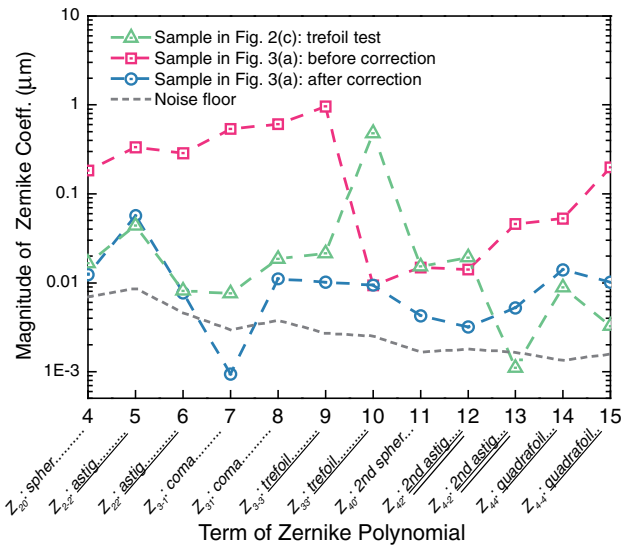


**Fig. 4.** Zernike coefficients of the measured deformations and surface profiles in Figs. 2 and 3. The dashed gray line represents the repeatability of our S-H metrology tool. The tilted text on the bottom indicates the IDs of the 12 Zernike terms. Letters without underline indicate terms that can be generated by equibiaxial stress, single underline for terms that can be generated by antibiaxial stress, and double underline for terms that require a combination of equibiaxial and antibiaxial stresses.

components can perfectly generate all Zernike terms over the entire substrate without edge effects. This is not the case if only equibiaxial stress can be controlled, which usually creates high-frequency residual errors. However, in practice, the magnitude of stress required to correct higher-order modes is large and we limit

our experiments to the first four orders (15 terms) of Zernike polynomials. Previous studies have shown that generating deformation with different Zernike terms requires different types of stresses. Among the 12 terms shown in Fig. 4, six of them need antibiaxial stress, four need equibiaxial stress, and two need a combination of both (Fig. S1). In this work, flattening surfaces by simultaneously minimizing 12 terms is a powerful demonstration of stress tensor manipulation. The measured surface before correction is the S shape in Fig. 3(a), with  $\sim 10 \mu\text{m}$  P-V, corresponding to the coefficients plotted by the magenta squares in Fig. 4. After calculation of the required stress tensor distribution based on an analytical solution and an FE model and taking into account the anisotropic elastic properties of silicon [30], Type-I mesostructures are designed (Fig. S11) and patterned [Fig. 3(b)] on the backside to provide adequate flattening stress tensors. Figure 3(c) shows the area between two unit cells, where the trenced lines are clearly visible. The flattened profile in Fig. 3(a) shows the measured surface after patterning, corresponding to the blue circles in Fig. 4, representing a RMS slope improvement factor of 27 (RMS height improvement factor of 21).

These results can benefit applications that only need one-time figuring. Figures 5 and 6 show results conducted by Type-II and Type-III structures that allow secondary forming and possibly active actuation [Eqs. (S7)–(S10)]. Figure 5(a) shows a microscope image of a patterned Type-II structure for trefoil deformation. The measured deformation in Fig. 5(b) shows the result is not perfect. As indicated by the arrow, a side lobe in the  $x$  direction is slightly higher, which is caused by an undesired astigmatism generated by the patterning process. This astigmatism component is clearly shown in the magenta squares in Fig. 7. Since the generated stress tensors can be adjusted after patterning due to the flexibility of

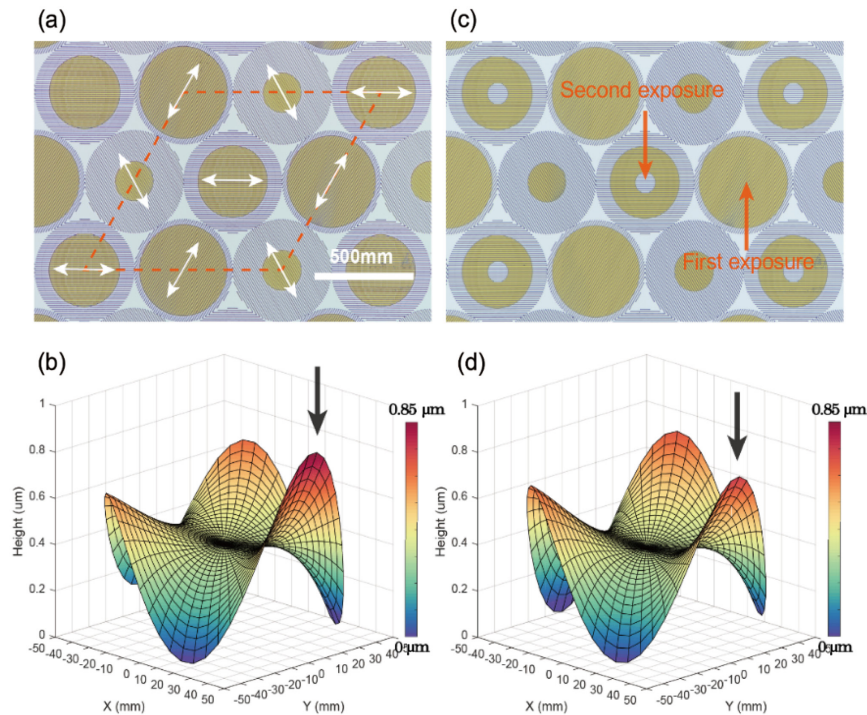


**Fig. 5.** Trefoil deformation of 100 mm silicon wafers generated by Type-II mesostructures patterned on back surfaces. (a) Microscope image of patterned Type-II mesostructures for trefoil deformation. Dashed lines indicate a unit cell, and the white arrows note the orientation of grating lines. (b) Measured trefoil deformation generated by (a). The dark arrow indicates that one of the generated side lobes is higher than expected, created by an undesired astigmatism term. (c) Microscope image of a Type-II mesostructure after secondary exposure. A portion of the TOx in grating disk centers with specific orientations is removed. (d) Measured trefoil deformation after the secondary exposure, showing that the side lobe indicated by the dark arrow is suppressed.

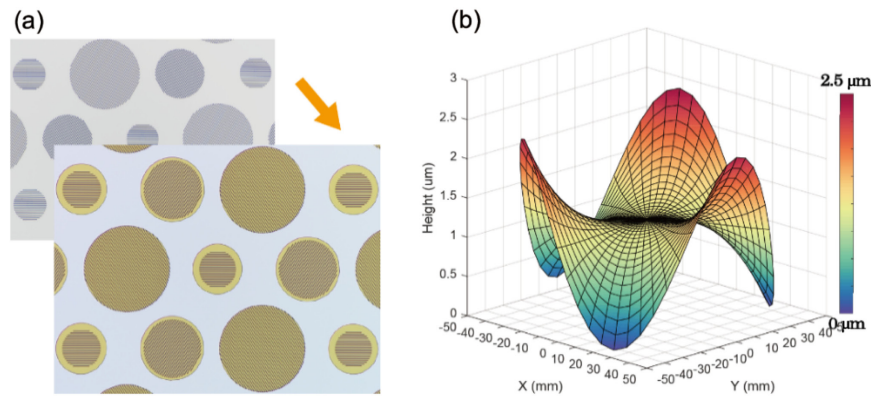


**Fig. 6.** (a) Microscope images of Type-III mesostructures. The background image is the silicon surface trench with grating lines before coating and patterning. The picture in the foreground shows patterned TOx layers on the top and the side of the grating tooth. (b) Measured trefoil deformation created by (a). The amplitude of the deformation is  $\sim 3\times$  higher than that produced by Type-II trefoil deformation of 100 mm silicon wafers generated by Type-II mesostructures patterned on back surfaces.

Type-II structures, we performed a secondary exposure to remove the undesired astigmatism. The TOx at the center of the disks, where the grating lines are along the  $x$  direction, was removed iteratively (Table S4), but without etching into the silicon [Fig. 5(c)]. Figure 5(d) shows the measured deformation after the secondary patterning, where the side-lobe amplitude has been suppressed. The Zernike coefficients plotted by the blue circles in Fig. 7 confirm that the generated trefoil has been improved. The capability of secondary adjustment granted by the Type-II structure can benefit the precision of the freeform process. In addition, the structure can enable actively controlled stress tensors for more applications, by switching the stress provider from TOx to ferromagnetic or piezoelectric materials.

Despite these advantages, comparing Figs. 2(c) and 5(d), the deformation amplitude produced by Type-II structures is only one-third of that produced by Type I due to the inefficient nature of the design. Figure 6(a) shows a Type-III structure for higher deformation amplitude with the same flexibility as Type II. Since the AR

of the grating lines is 1.0, which provides three times the coating area, the generated deformation in Fig. 6(b) shows an amplitude  $\sim 3$  times higher than Type II, as expected.

### 5. SUMMARY

In summary, we have presented three types of stress mesostructures that can manipulate the general stress tensor on thin substrates to create precise freeform deformations not achievable by conventional methods. Type-I patterns should be used when the deformation provided by Type-II and Type-III patterns is insufficient. However, Type-II and Type-III patterns may enable multiple-pass corrections because each stress component can be controlled by adjusting the area of remaining TOx, whereas the angle  $\phi$  in the Type-I pattern cannot be adjusted after patterning. Type-III patterns require additional processing steps but provide higher stress than Type II. The mesostructures are compatible with modern planar fabrication technologies, which have the potential to be scaled and extended for a wide range of applications including active actuation of thin substrates in the future.

**Funding.** National Aeronautics and Space Administration (80NSSC20K0907, NNX14AE76G, NNX17AE47G).

**Disclosures.** The authors declare no conflicts of interest.

**Data availability.** All data are available in the main text and the Supplement 1.

**Supplemental document.** See Supplement 1 for supporting content.

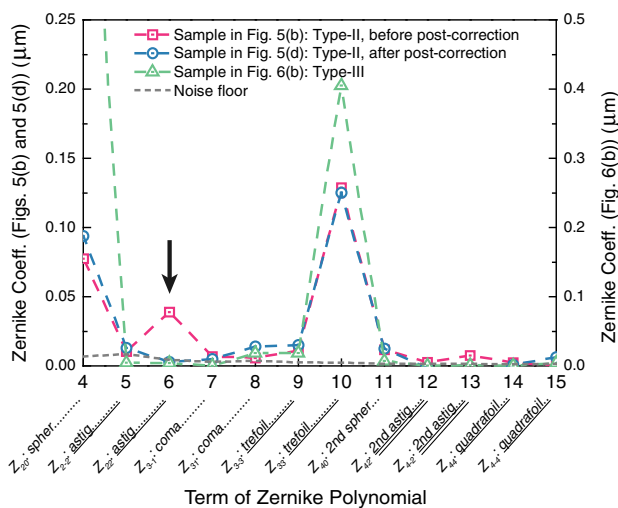


**Fig. 7.** Zernike coefficients of the measured deformations and surface profiles in Figs. 5(b), 5(d), and 6(b). The dashed gray line represents the repeatability of our S-H metrology tool. The tilted text on the bottom indicates the IDs of the 12 Zernike terms. Letters without underline indicate terms that can be generated by equibiaxial stress, single underline for terms that can be generated by antibiaxial stress, and double underline for terms that require a combination of equibiaxial and antibiaxial stresses.

### REFERENCES

1. D. K. Nikolov, A. Bauer, F. Cheng, H. Kato, A. N. Vamivakas, and J. P. Rolland, "Metaform optics: bridging nanophotonics and freeform optics," *Sci. Adv.* **7**, eabe5112 (2021).
2. M. Khorasaninejad and F. Capasso, "Metalenses: versatile multifunctional photonic components," *Science* **358**, eaam8100 (2017).
3. A. She, S. Zhang, S. Shian, D. R. Clarke, and F. Capasso, "Large area metalenses: design, characterization, and mass manufacturing," *Opt. Express* **26**, 1573–1585 (2018).
4. F. Z. Fang, X. D. Zhang, A. Weckenmann, G. X. Zhang, and C. Evans, "Manufacturing and measurement of freeform optics," *CIRP Ann.* **62**, 823–846 (2013).
5. B. Kress and T. Starner, "A review of head-mounted displays (HMD) technologies and applications for consumer electronics," *Proc. SPIE* **8720**, 87200A (2013).

6. L. Keesey, NASA, "NASA's new lightweight x-ray mirrors ready for try-outs in space," 2019, <https://www.nasa.gov/feature/goddard/2019/nasa-s-new-lightweight-x-ray-mirrors-ready-for-try-outs-in-space>.
7. N. Nakaniwa, Y. Ezoe, M. Numazawa, M. Takeo, M. Ishida, K. Ishikawa, K. Morishita, and K. Nakajima, "Development of x-ray mirror foils using a hot plastic deformation process," *Appl. Opt.* **59**, 8793–8805 (2020).
8. B. D. Chalifoux, R. K. Heilmann, H. L. Marshall, and M. L. Schattenburg, "Optical design of diffraction-limited x-ray telescopes," *Appl. Opt.* **59**, 4901–4914 (2020).
9. S. Cai, C. Zhang, H. Li, S. Lu, Y. Li, K. Hwang, and X. Feng, "Surface evolution and stability transition of silicon wafer subjected to nano-diamond grinding," *AIP Adv.* **7**, 035221 (2017).
10. J. Walker, T. Liu, M. Tendulkar, D. N. Burrows, C. T. Deroo, R. Allured, E. N. Hertz, V. Cotroneo, P. B. Reid, E. D. Schwartz, T. N. Jackson, and S. Trolter-Mckinstry, "Design and fabrication of prototype piezoelectric adjustable x-ray mirrors," *Opt. Express* **26**, 27757–27772 (2018).
11. X. Wang, Y. Yao, T. Liu, C. Liu, M. Ulmer, and J. Cao, "Deformation of rectangular thin glass plate coated with magnetostrictive material," *Smart Mater. Struct.* **25**, 085038 (2016).
12. M. Lepedus, "3D NAND's vertical scaling race," 2020, <https://semiengineering.com/3d-nands-vertical-scaling-race/>.
13. D. Shi, Z. Xia, M. Hu, G. Mei, and Z. Huo, "A novel solution to improve saddle-shape warpage in 3D NAND flash memory," *Semicond. Sci. Technol.* **35**, 045031 (2020).
14. M. Ghigo, S. Basso, M. Civitani, R. Gilli, G. Paraschi, B. Salmaso, G. Vecchi, and W. W. Zhang, "Final correction by ion beam figuring of thin shells for x-ray telescopes," *Proc. SPIE* **10706**, 1070631 (2018).
15. B. D. Chalifoux, C. Burch, R. K. Heilmann, Y. Yao, H. Zuo, and M. L. Schattenburg, "Using ion implantation for figure correction in glass and silicon mirror substrates for x-ray telescopes," *Proc. SPIE* **10399**, 103991D (2017).
16. U. M. Khazi and U. Mescheder, "3D free forms in c-Si via grayscale lithography and RIE," *Microelectron. Eng.* **193**, 34–40 (2018).
17. H. An, Y. Park, K. Kim, Y. Nam, M. Song, and J. Park, "High-resolution 3D printing of freeform, transparent displays in ambient air," *Adv. Sci.* **6**, 1901603 (2019).
18. Y. Yao, B. D. Chalifoux, R. K. Heilmann, and M. L. Schattenburg, "Thermal oxide patterning method for compensating coating stress in silicon substrates," *Opt. Express* **27**, 1010–1024 (2019).
19. Y. Yao, B. D. Chalifoux, R. K. Heilmann, K. W. Chan, H. Mori, T. Okajima, W. W. Zhang, and M. L. Schattenburg, "Progress of coating stress compensation of silicon mirrors for Lynx x-ray telescope mission concept using thermal oxide patterning method," *J. Astron. Telescopes Instrum. Syst.* **5**, 021011 (2019).
20. Y. Yao, X. Wang, J. Cao, and M. P. Ulmer, "Stress manipulated coating for fabricating lightweight x-ray telescope mirrors," *Opt. Express* **23**, 28605–28618 (2015).
21. S. Verpoort and U. Wittrock, "Actuator patterns for unimorph and bimorph deformable mirrors," *Appl. Opt.* **49**, G37–46 (2010).
22. B. D. Chalifoux, R. K. Heilmann, and M. L. Schattenburg, "Correcting flat mirrors with surface stress: analytical stress fields," *J. Opt. Soc. Am.* **35**, 1705–1716 (2018).
23. C. Beckmann and J. Ihlemann, "Figure correction of borosilicate glass substrates by nanosecond UV excimer laser irradiation," *Opt. Express* **28**, 18681–18692 (2020).
24. Y. Kim, H. Yuk, R. Zhao, S. Chester, and X. Zhao, "Printing ferromagnetic domains for untethered fast-transforming soft materials," *Nature* **558**, 274–281 (2018).
25. H. Cui, R. Hensleigh, D. Yao, D. Maurya, P. Kumar, M. G. Kang, S. Priya, and X. Zheng, "Three-dimensional printing of piezoelectric materials with designed anisotropy and directional response," *Nat. Mater.* **18**, 234–241 (2019).
26. Freund and S. Suresh, *Thin Film Materials: Stress, Defect Formation and Surface Evolution* (Cambridge University, 2003), p. 205.
27. C. Forest, C. Canizares, D. Neal, M. McGuirk, A. Slocum, and M. L. Schattenburg, "Metrology of thin transparent optics using Shack-Hartmann wavefront sensing," *Opt. Eng.* **43**, 742–753 (2004).
28. M. Akilian, C. Forest, A. Slocum, D. Trumper, and M. L. Schattenburg, "Thin optic constraint," *Precis. Eng.* **31**, 130–138 (2006).
29. B. D. Chalifoux, E. Sung, R. K. Heilmann, and M. L. Schattenburg, "High-precision figure correction of x-ray telescope optics using ion implantation," *Proc. SPIE* **8861**, 88610T (2013).
30. M. A. Hopcroft, W. D. Nix, and T. W. Kenny, "What is the Young's modulus of silicon?" *J. Microelectromech. Syst.* **19**, 229–238 (2010).